Research Square

Preprints are preliminary reports that have not undergone peer review. They should not be considered conclusive, used to inform clinical practice, or referenced by the media as validated information.

Repurposing TACE-Induced Hypoxia to Activate Biocatalytic Hydrogen Production and Potentiate Tirapazamine Chemoimmunotherapy Against Hepatocellular Carcinoma

Xiangyu Lu
Sichuan Academy of Medical Sciences, Sichuan Provincial People's Hospital, University of Electronic Science and Technology of China

Yuefeng He
Sichuan Academy of Medical Sciences, Sichuan Provincial People's Hospital, University of Electronic Science and Technology of China

Yu He
Sichuan Academy of Medical Sciences, Sichuan Provincial People's Hospital, School of Medicine, University of Electronic Science and Technology of China

Renjie Liang
Sichuan Academy of Medical Sciences, Sichuan Provincial People's Hospital, School of Medicine, University of Electronic Science and Technology of China

Wenhao Li
Sichuan Academy of Medical Sciences, Sichuan Provincial People's Hospital, School of Medicine, University of Electronic Science and Technology of China

Shi Zhou
Affiliated Hospital of Guizhou Medical University

Xiaoshuang Chen
West China Hospital, Sichuan University

Yue Zhu
Sichuan Academy of Medical Sciences, Sichuan Provincial People's Hospital, University of Electronic Science and Technology of China

Lei Cao
caolei@med.uestc.edu.cn

Sichuan Academy of Medical Sciences, Sichuan Provincial People's Hospital, School of Medicine, University of Electronic Science and Technology of China

---

Research Article

Keywords: Hepatocellular carcinoma, TACE, synechocystis, tirapazamine, chemoimmunotherapy

Posted Date: October 16th, 2026

DOI: https://doi.org/10.21203/rs.3.rs-11251678/v1

License: This work is licensed under a Creative Commons Attribution 4.0 International License. Read Full License

Additional Declarations: No competing interests reported.

Abstract

Transcatheter arterial chemoembolization (TACE) is a first-line therapy for advanced hepatocellular carcinoma (HCC), however, embolization-induced tumor hypoxia frequently promotes drug resistance and recurrence. To convert this hypoxic stress into a therapeutic opportunity, we constructed hyaluronidase-degradable microspheres (Sp/TPZ@MNs) co-encapsulating live Synechocystis (Sp) for biohydrogen production and tirapazamine (TPZ), a hypoxia-activated prodrug. Upon embolization, the resultant hypoxic microenvironment triggers endogenous hydrogenase-mediated H_2 generation from Sp and simultaneously activates TPZ. The evolved H_2 potentiates TPZ-induced DNA damage, eliciting robust immunogenic cell death (ICD), which subsequently promotes dendritic cell maturation and M1 polarization of tumor-associated macrophages. In vitro, Sp/TPZ@MNs under hypoxia significantly enhanced HepG2 cell killing and immune activation. In a rabbit orthotopic Vx2 HCC model, the microspheres exhibited favorable injectability, embolization performance, and enzyme-responsive degradation, leading to marked tumor growth suppression and reduced pulmonary metastasis with good biosafety. This cascade strategy converts hypoxic stress into a therapeutic asset, offering a novel paradigm for TACE potentiation.

Introduction

Hepatocellular carcinoma (HCC) ranks among the most lethal malignancies worldwide, with most patients diagnosed at intermediate or advanced stages when curative resection is no longer feasible[1–3]. Transcatheter arterial chemoembolization (TACE) has been established as the first-line locoregional therapy for unresectable HCC, achieving tumor control through dual mechanisms of ischemic devascularization and localized chemotherapeutic drug delivery[4–6]. Despite widespread clinical implementation, TACE suffers from unsatisfactory therapeutic durability[7–9]. Tumor hypoxia inevitably develops following vascular occlusion upon embolization, and such hypoxic microenvironment frequently fuels adaptive metabolic reprogramming, epithelial-mesenchymal transition, as well as multidrug resistance[10–12]. These pathological events collectively contribute to tumor recurrence and distant metastasis[13–15]. This inherent paradox is that hypoxia generated by TACE itself counteracts therapeutic benefits of this intervention. It constitutes a persistent bottleneck that conventional embolic agents have failed to address.

Hypoxia-activated prodrugs (HAPs), exemplified by tirapazamine (TPZ), have emerged as a promising class of agents that selectively generate cytotoxic DNA-damaging radicals under hypoxic conditions, theoretically offering a means to exploit rather than merely tolerate tumor hypoxia[16–18]. However, clinical translation of TPZ has been hampered by insufficient intratumoral hypoxia intensity and heterogeneous oxygen distribution, which limit prodrug bioactivation to only a narrow perinecrotic zone[19–21]. Biohydrogen has been reported to potentiate genotoxic drug-triggered tumor cell damage, inspiring us to seek biological platforms for in-situ hydrogen generation within tumor lesions[22–24]. Living microorganisms, especially photosynthetic cyanobacteria, feature notable metabolic plasticity[25]. Under

anaerobic conditions, Synechocystis (Sp) elevates endogenous hydrogenase activity and produces biohydrogen via fermentative metabolism[26–28]. We therefore hypothesized that embedding viable Sp within embolic microspheres would enable a cooperative therapeutic cascade. Embolization-induced intratumoral hypoxia triggers concurrent TPZ prodrug activation and cyanobacteria-mediated biohydrogen biosynthesis, where

the metabolically generated hydrogen serves as a synergistic effector to augment TPZ-mediated antitumor responses. In this way, the hypoxia induced by TACE is repurposed as a shared trigger to coordinate two independent therapeutic moieties, converting the detrimental hypoxic stress of TACE into a therapeutic asset.

Herein, we report hyaluronidase-degradable embolic microspheres (Sp/TPZ@MNs) that co-encapsulate living Sp and TPZ for cascade-amplified TACE of HCC. The microspheres preserve cyanobacterial viability and hydrogenase-mediated biocatalytic activity while exhibiting favorable injectability, rheological behavior, and enzyme-responsive degradation (Fig. 1A). Under hypoxic conditions, Sp-derived biohydrogen cooperates with activated TPZ to induce robust DNA damage and immunogenic cell death (ICD), accompanied by DAMPs release, dendritic cell maturation, and M1-type macrophage polarization (Fig. 1B). In rabbit orthotopic Vx2 HCC models, Sp/TPZ@MNs-mediated TACE achieves effective vascular embolization, markedly suppresses tumor growth and pulmonary metastasis, and remodels the tumor immune microenvironment; transcriptomic profiling reveals significant perturbations in cAMP, interferon, and arachidonic acid metabolic pathways. This work establishes a cascade therapeutic paradigm that harnesses living cyanobacterial metabolism to turn TACE-induced hypoxia from a liability into a leveraged therapeutic trigger, offering a broadly applicable strategy for potentiating embolic cancer therapy.

Results

Construction and physicochemical characterization of Sp/TPZ@MNs

Scanning electron microscopy (SEM) was first applied to characterize the morphology of cultured Sp. As shown in Fig. 2A, B, Sp cells displayed regular spherical geometry with uniform surface texture, and the statistical particle-size distribution demonstrated an average diameter around 2 μm (Fig. 2C). Owing to intrinsic phycobiliprotein pigments, Sp exhibited spontaneous red autofluorescence under laser confocal scanning microscopy, which enables direct visual tracking without additional fluorescent labeling (Fig. 2D). Given that hydrogen production of cyanobacteria is strictly oxygen-dependent, we further established an in-vitro gas-collection system coupled with gas-phase mass spectrometry to monitor fermentative hydrogen generation under different atmospheric conditions (Fig. 2E). Substantial cumulative hydrogen was continuously detected under nitrogen-purged anaerobic conditions, whereas negligible hydrogen yield was recorded under oxygen-rich atmosphere, verifying that hydrogenase-mediated biocatalytic hydrogen production of Sp is only triggered upon oxygen deprivation

(Fig. 2F). Methylene blue (MB) redox-sensitive UV-vis spectroscopy further supported this observation: obvious fading of MB

absorbance was observed exclusively in anaerobic Sp-containing groups, reflecting the accumulation of reducing metabolites generated during Sp anaerobic metabolism (Fig. 2G).

Having confirmed the anaerobic-triggered hydrogen-producing capability of free Sp, we next fabricated hyaluronidase-degradable embolic microspheres co-encapsulating living Sp and hypoxia-activated prodrug TPZ, designated Sp/TPZ@MNs. Optical microscopy and SEM images illustrated that Sp/TPZ@MNs maintained well-defined spherical shape after material fabrication, with a suitable particle-size window favorable for transcatheter arterial embolization (Fig. 2H**-K** and **Fig. S1**). To visualize the spatial distribution of payloads inside microspheres, TPZ was substituted with FITC for confocal observation. The merged confocal images exhibited overlapping red fluorescence from Sp and green FITC signal throughout the microsphere matrix, confirming homogeneous co-loading of both biological and small-molecule payloads (Fig. 2L). Encapsulation-associated cytotoxicity is a major concern for living-cell-embedded biomaterials. Therefore, we compared cell viability and hydrogen-generating capacity between free Sp and microsphere-encapsulated Sp after 48 h incubation. No significant difference in Sp survival rate was observed between the two groups, and encapsulated Sp retained comparable hydrogen-producing activity (Fig. 2M, N). These data indicated that the microsphere polymer matrix provides a biocompatible microenvironment to preserve the metabolic function of embedded cyanobacteria.

Subsequently, enzyme-responsive degradation, injectability and mechanical performance, which are critical prerequisites for TACE embolic agents, were systematically evaluated. Sp/TPZ@MNs displayed time-dependent degradation behavior in the presence of hyaluronidase, and higher enzyme concentration accelerated microsphere erosion (Fig. 2O). Such enzyme-driven degradation further enabled the responsive release of encapsulated TPZ from the decomposing microspheres (**Fig. S2**). Rheological measurements revealed typical shear-thinning viscosity profiles of Sp/TPZ@MNs upon increasing shear rate, which is essential for smooth delivery through clinical microcatheters. The storage modulus (G') and loss modulus (G") of Sp/TPZ@MNs were comparable to blank microspheres without Sp and TPZ, suggesting that payload incorporation did not alter the viscoelastic properties of the base material (Fig. 2P, Q). Compression force-deformation curves further demonstrated adequate mechanical tolerance of Sp/TPZ@MNs under mechanical compression (Fig. 2R). Collectively, these physicochemical characterizations corroborate that Sp/TPZ@MNs satisfy key requirements for embolic application: stable co-encapsulation of functional living cyanobacteria and TPZ prodrug, hyaluronidase-responsive degradation, favorable rheological property and mechanical robustness for catheter-based interventional delivery.

In vitro antitumor effects of Sp/TPZ@MNs

After validating the physicochemical performance of Sp/TPZ@MNs, we moved on to explore its in-vitro antitumor potency against HepG2 hepatocellular carcinoma cells under normoxic and hypoxic culture conditions. As illustrated in the schematic of Fig. 3A, the TACE-mimicking hypoxic microenvironment concurrently enables Sp-driven biohydrogen biosynthesis and TPZ prodrug activation. The resulting biohydrogen synergizes with activated TPZ to elicit tumor cell damage. Consistently, experimental hydrogen-quantification results showed prominent hydrogen accumulation only in Sp-containing groups under hypoxic incubation, while normoxic groups and Sp-free formulations generated barely detectable hydrogen (Fig. 3B). CCK-8 cell viability assays were then performed to assess tumor-cell killing capacity. Under normoxia, all experimental groups exhibited limited cytotoxicity toward HepG2

cells. In sharp contrast, under hypoxic conditions, Sp/TPZ@MNs exerted markedly enhanced tumor-cell suppression, outperforming single-component groups including Sp@Ms and TPZ@Ms (Fig. 3C). Flow-cytometry-based apoptosis detection and live/dead confocal staining further recapitulated this tendency. The highest proportion of apoptotic and dead tumor cells was observed exclusively in the Sp/TPZ@MNs hypoxia group, while other treatment groups only induced moderate or trivial cell death (Fig. 3D, E and **Fig. S3**). To dissect the underlying cell-death mechanism, DNA-damage marker γH2AX and mitochondrial membrane potential (ΔΨm) were detected. Under normoxic conditions, all groups showed low γH2AX fluorescence intensity. Once exposed to hypoxia, Sp/TPZ@MNs treatment induced massive γH2AX foci formation, indicating severe DNA double-strand breaks (Fig. 3F, G). Mitochondrial injury is another hallmark of TPZ-mediated cytotoxicity. JC-1 staining illustrated obvious mitochondrial depolarization in hypoxic Sp/TPZ@MNs group, manifested as decreased red-to-green fluorescence ratio (Fig. 3H, I). Taken together, these cellular observations suggest that hypoxia-driven hydrogen production cooperates with activated TPZ to provoke DNA damage and mitochondrial dysfunction, jointly amplifying the death of HepG2 tumor cells.

Induction of ICD in HepG2 cells

Given the potent cytotoxicity elicited by Sp/TPZ@MNs under hypoxic conditions, we further explored whether the observed tumor-cell death corresponded to an ICD phenotype. Immunofluorescence staining was performed to assess three well-established ICD markers, including surface-exposed calreticulin (CRT), secreted HMGB1, and HSP70[29]. Under normoxic circumstances, only faint signal of these DAMPs could be detected across all groups. Hypoxic Sp/TPZ@MNs treatment remarkably promoted CRT translocation onto cell membrane, as well as the extracellular release of HMGB1 and HSP70 (Fig. 4A**-F**). These results preliminarily demonstrated that Sp/TPZ@MNs could trigger robust ICD in hypoxic HepG2 cells. We further constructed tumor-cell-antigen-presenting-cell co-culture systems to verify the downstream immune-activating effect of ICD. Tumor-cell-conditioned medium collected from hypoxic Sp/TPZ@MNs treatment remarkably promoted M1-type

polarization of tumor-associated macrophages (TAMs), whereas immunosuppressive M2-macrophage proportion declined correspondingly (Fig. 4G). Meanwhile, ELISA results revealed decreased secretion of

M2-related immunosuppressive chemokines CCL22 and IL-10 (Fig. 4H, I). When dendritic cells (DCs) were co-incubated with pretreated HepG2 cells, DC maturation was significantly elevated in the Sp/TPZ@MNs hypoxia group, accompanied by higher secretion of pro-inflammatory cytokines TNF-α and IL-6 (Fig. 4J**-L**). Collectively, these co-culture experiments confirm that Sp/TPZ@MNs-triggered ICD is biologically functional, which facilitates macrophage reprogramming and DC maturation, laying the foundation for subsequent antitumor immune activation.

Embolization performance and in vivo biosafety of Sp/TPZ@MNs

Encouraged by promising in-vitro results, we shifted to rabbit orthotopic Vx2 HCC models, which are widely accepted preclinical large-animal models for TACE evaluation. We adopted an optical tissue-clearing strategy to intuitively visualize the intratumoral retention and distribution of Sp/TPZ@MNs after interventional embolization **(**Fig. 5A, B). Ex-vivo cleared liver specimens exhibited strong red autofluorescence signals originating from Sp, predominantly localized within tumor lesions, proving that Sp/TPZ@MNs could be smoothly delivered via interventional catheter and efficiently trapped inside tumor-feeding vessels to achieve regional embolization (Fig. 5C, D). Immunofluorescence sections further displayed obvious Sp-derived autofluorescence in tumor parenchyma, validating successful tumor embolization (**Fig. S4**). H&E staining further evidenced massive tumor cell death post-embolization (**Fig. S5**).

In-vivo biosafety is a critical evaluation indicator for embolic biomaterials before further translational study. Blood serum biochemical indices covering liver function (ALT, AST), kidney function (BUN, Cre), and routine blood biochemistry parameters were monitored at predefined time-points after Sp/TPZ@MNs-mediated TACE. Throughout the 30-day observation period, serum biochemical indicators remained within normal physiological ranges without obvious abnormal fluctuations (Fig. 5E). Moreover, H&E histological staining of major organs including heart, liver, spleen,

lung and kidney displayed no noticeable inflammatory infiltration, tissue necrosis or pathological damage (Fig. 5F). Combining embolization imaging data and biosafety assessments, Sp/TPZ@MNs achieves satisfactory tumor-vascular embolization capacity with favorable systemic biocompatibility in tumor-bearing rabbits.

In vivo antitumor efficacy against orthotopic HCC

Subsequently, systematic in-vivo therapeutic efficacy assessment was performed on rabbit orthotopic Vx2 HCC after different TACE treatments. The schematic diagram (Fig. 6A) illustrates the interventional TACE procedure implemented in this study. TACE treatment was initiated when orthotopic liver tumors reached longitudinal and transverse dimensions of ~ 1.27 cm and ~ 0.78 cm, as confirmed by ultrasound imaging (**Fig. S6**). Tumor-tissue H&E staining revealed extensive coagulative necrosis inside tumor lesions for the Sp/TPZ@MNs treatment group. By contrast, blank-Ms, Sp@Ms and TPZ@Ms groups only

generated partial tumor necrosis, indicating superior tumor-killing effects of combined Sp-hydrogen and TPZ therapy (Fig. 6B). Serial T2-weighted magnetic resonance imaging was conducted to dynamically monitor tumor growth. For control and single-treatment groups, tumor volume continuously increased over 14 days post-TACE. On the contrary, obvious tumor shrinkage was observed in the Sp/TPZ@MNs cohort (Fig. 6C). Quantitative tumor-volume statistics, both average tumor-growth curves and individual tumor-volume variation, further quantified the potent tumor-suppression effect achieved by Sp/TPZ@MNs-based TACE (Fig. 6D, E).

To further characterize intratumor pathological alterations, tumor-tissue immunofluorescence staining of HIF-α, TUNEL and Ki-67 was carried out. HIF-α serves as the canonical marker reflecting intratumoral hypoxic status. Although TACE itself blocks blood supply, Sp/TPZ@MNs treatment significantly downregulated intratumoral HIF-α expression (**Fig. S7**). Meanwhile, increased TUNEL-positive

apoptotic signals and reduced Ki-67 proliferative signals were detected in Sp/TPZ@MNs tumor sections (Fig. 6F, G and **Fig. S8-9**). These histological findings demonstrate that Sp/TPZ@MNs-mediated TACE induces robust tumor-cell apoptosis, suppresses tumor proliferation and alters intratumoral hypoxic signaling, leading to potent therapeutic outcomes in this large-animal HCC model.

Remodeling of the tumor immune microenvironment

Our in-vitro data had proven that Sp/TPZ@MNs could trigger ICD and activate antigen-presenting cells. We therefore sought to verify whether such immune-activating effects could be recapitulated in vivo within orthotopic tumor tissues. Immunohistochemical staining of tumor sections demonstrated significantly elevated intratumoral CRT, HMGB1 and HSP70 expression in Sp/TPZ@MNs group compared with other cohorts, confirming in-situ ICD occurrence after TACE treatment (Fig. 7A).

Tumor-tissue flow cytometry was next performed to dissect immune-cell infiltration profiles. Sp/TPZ@MNs treatment markedly raised the proportion of mature DCs inside tumor tissue. For tumor-associated macrophages, the percentage of anti-tumor M1-type TAMs increased, while pro-tumor M2-type TAMs declined. Furthermore, the infiltration of cytotoxic $CD8^+$ T cells, which execute core antitumor immune function, was obviously elevated in Sp/TPZ@MNs-treated tumors (Fig. 7B**-E**). Confocal immunofluorescence imaging of tumor sections further visually validated these changes: more $F4/80^+iNOS^+$ M1 macrophages and $CD3^+CD8^+$ T cells accumulated in tumor sites of Sp/TPZ@MNs group (Fig. 7F, G).

Given the reshaped antitumor immune microenvironment, we further assessed pulmonary metastasis, a frequent malignant progression pattern for HCC. H&E staining of lung tissues showed obviously decreased metastatic-nodule burden in Sp/TPZ@MNs-treated rabbits (Fig. 7H, I). These results collectively illustrate that Sp/TPZ@MNs-provoked ICD remodels the intrinsically immunosuppressive HCC tumor microenvironment, promotes intratumoral cytotoxic immune-cell infiltration, and consequently restrains tumor distant metastasis.

Transcriptomic analysis of the underlying mechanisms

To gain deeper mechanistic insights into the molecular events elicited by Sp/TPZ@MNs-based TACE, we implemented transcriptome RNA-sequencing analysis on tumor tissues collected from control and Sp/TPZ@MNs groups. The overall

workflow for sample collection and sequencing is outlined in Fig. 8A. Differential-gene-expression analysis identified hundreds of significantly altered genes ($|\log_2 FC| > 1$, $P < 0.05$), visualized by volcano plot and gene-expression heatmap (Fig. 8B, C). KEGG pathway enrichment bubble plots for upregulated and downregulated differentially expressed genes uncovered multiple enriched metabolism- and immune-relevant signaling pathways (Fig. 8D, E). Gene-ontology (GO) functional enrichment further annotated the biological-process, cellular-component and molecular-function categories perturbed upon Sp/TPZ@MNs intervention (Fig. 8F). Gene set enrichment analysis (GSEA) was further applied to pinpoint key altered pathways. Among them, cAMP signaling pathway, interferon signaling pathway and arachidonic-acid metabolism exhibited prominent enrichment differences between two groups (Fig. 8G**-I**). The interferon signaling pathway is tightly associated with antitumor immune activation, while cAMP and arachidonic-acid metabolism participate in tumor-cell survival, inflammation and immune-microenvironment modulation. Consistent with these transcriptomic alterations, we further performed ELISA quantification of key inflammatory and immune-related cytokines derived from tumor-bearing rabbit tissues. These protein-level measurements corroborated the transcriptome-predicted immune-activating phenotype, showing elevated levels of pro-inflammatory antitumor cytokines alongside reduced concentrations of immunosuppressive mediators (**Fig. S10**). Collectively, these transcriptomic signatures together with supporting cytokine profiling provide multi-layered molecular-level evidence explaining the chemo-immunotherapeutic synergistic effects triggered by Sp/TPZ@MNs in orthotopic HCC.

Discussion

TACE represents the standard-of-care locoregional therapeutic option for intermediate-stage HCC[30]. Embolism-triggered intratumoral hypoxia gives rise to a notable biological paradox[31]. While hypoxia contributes to ischemic tumor necrosis, it also promotes drug resistance, malignant progression, and the formation of an immunosuppressive tumor microenvironment, which substantially impairs clinical therapeutic responses. Numerous strategies have been proposed to counteract TACE-related hypoxia, including oxygen-carrying embolic agents, hypoxia-targeted small-molecule drugs and hypoxia-activated prodrugs[1]. Among them, TPZ represents a well-investigated hypoxia-activated prodrug that generates cytotoxic DNA-damaging radicals selectively under low-oxygen conditions. Nevertheless, insufficient and heterogeneous hypoxia within solid tumors restricts the in-vivo activation efficiency of TPZ, and single-agent TPZ hardly achieves satisfactory therapeutic benefits, which hinders its clinical translation.

In this work, we constructed hyaluronidase-degradable embolic microspheres (Sp/TPZ@MNs) co-encapsulating living Sp and TPZ, which repurposes TACE-induced hypoxia as a shared trigger for dual

therapeutic modules, rather than simply eliminating tumor hypoxia. Once embolization blocks tumor blood supply, the formed hypoxic niche simultaneously initiates cyanobacterial biocatalytic hydrogen production and TPZ prodrug activation. Instead of aggravating tumor hypoxia, the biosynthesized hydrogen acts as a synergistic effector to amplify TPZ-mediated DNA damage, further triggering robust immunogenic cell death and subsequent antitumor immune responses. Different from previously reported oxygen-supplement embolic materials aiming to relieve hypoxia, our design makes use of the unavoidable hypoxic stress after TACE to activate two independent therapeutic moieties, offering an alternative logic for TACE-based combination therapy.

Living microbial-based biomaterials have attracted increasing attention for oncological therapy; however, most reported cyanobacteria-based tumor-therapeutic systems are applied via intratumoral or intravenous injection, and few integrate living cyanobacteria into clinical-applicable embolic microspheres for interventional TACE therapy. The physicochemical characterizations in Fig. 2 verified that Sp/TPZ@MNs possess appropriate particle size, shear-thinning rheological property and enzyme-responsive degradability for catheter delivery. Critically, the polymer matrix maintains the viability and hydrogen-producing biocatalytic activity of encapsulated Sp, which is the prerequisite for subsequent cascade therapeutic effects. In vitro cellular assays validated that Sp-derived hydrogen cooperates with activated TPZ to induce DNA damage, mitochondrial dysfunction and potent ICD, which drives macrophage M1-polarization and dendritic cell maturation (Fig. 3**-4**). The rabbit orthotopic Vx2 HCC model, a clinically-relevant large-animal pre-clinical model for TACE evaluation, further demonstrated that Sp/TPZ@MNs-mediated TACE achieves effective vascular embolization, potent tumor suppression and reduced pulmonary metastasis without obvious systemic toxicity (Fig. 5**-7**).

Transcriptome sequencing further uncovered the molecular mechanisms behind therapeutic benefits. Sp/TPZ@MNs treatment significantly modulated cAMP signaling, interferon signaling and arachidonic acid metabolism pathways. Interferon pathway activation is consistent with the observed intratumoral immune-cell infiltration and ICD-driven antitumor immunity, while cAMP and arachidonic acid metabolism participate in tumor proliferation, inflammation and immune microenvironment regulation. Supporting-information cytokine ELISA data further supplied protein-level evidence for immune activation, consolidating the multi-omics and phenotypic results.

Nevertheless, several limitations still exist in the current study. First, although Sp survives and executes fermentative hydrogen production inside microspheres under tumor hypoxic conditions, the long-term in-vivo metabolic stability and persistence of Sp after TACE still need further optimization. Second, this study adopts the Vx2 rabbit liver tumor model; future validation in immunocompetent genetically-engineered HCC mouse models will help better interpret adaptive antitumor immune responses. Third, the exact molecular mechanism by which hydrogen potentiates TPZ cytotoxicity remains incompletely clarified. Follow-up mechanistic investigations are required to illustrate how hydrogen reshapes cellular redox homeostasis to amplify TPZ-triggered DNA injury. In addition, further fine-tuning of microsphere degradation kinetics and payload loading efficiency will benefit future translational studies.

Despite above-mentioned drawbacks, the present work proves the feasibility of integrating living cyanobacterial biocatalysis with hypoxia-activated prodrug into functional embolic microspheres. This cascade strategy converts TACE-derived harmful hypoxic stress into a therapeutic trigger, which may provide new insights for developing next-generation TACE embolic formulations for HCC treatment.

Conclusion

In summary, we report hyaluronidase-degradable embolic microspheres Sp/TPZ@MNs co-encapsulating living Sp and TPZ for cascade-synergistic TACE therapy of hepatocellular carcinoma. Upon arterial embolization, TACE-induced hypoxia serves as a shared switch to trigger cyanobacterial biocatalytic hydrogen generation and TPZ prodrug activation. The generated hydrogen synergistically potentiates TPZ-provoked DNA damage and elicits robust immunogenic cell death. In vitro experiments demonstrated that Sp/TPZ@MNs under hypoxic conditions effectively kill HCC tumor cells and activate antigen-presenting cells to initiate antitumor immune responses. In rabbit orthotopic Vx2 HCC models, Sp/TPZ@MNs realize favorable embolization performance, markedly suppress tumor growth and pulmonary metastasis with satisfying biosafety. Transcriptomic profiling combined with supporting cytokine ELISA results reveal the perturbation of multiple immune- and metabolism-related signaling pathways after Sp/TPZ@MNs intervention. This study establishes a proof-of-concept strategy that harnesses TACE-intrinsic hypoxia to activate dual therapeutic modules of living-microbe-derived biohydrogen and hypoxia-activated prodrugs, offering a prospective blueprint for designing advanced embolic agents against hepatocellular carcinoma.

Declarations

Ethics approval and consent to participate

All animal experiments were permitted by the Animal Care and Use Committee of Sichuan Provincial People’s Hospital. All procedures were in accordance with the protocols permitted by the Animal Research Center of Sichuan Provincial People’s Hospital.

Consent for publication

Not applicable.

Competing interests

The authors declare no competing interests.

Author Contribution

X.L., Y.F.H., and Y.H. designed and performed the main experiments, analyzed the data, and wrote the main manuscript text. R.L., W.L., and S.Z. assisted with the in vitro and in vivo experiments, data collection, and prepared the figures. X.C., Y.Z., and L.C. conceptualized the study, acquired funding, supervised the research, and critically revised the manuscript. All authors reviewed the manuscript.

Acknowledgement

Xiangyu Lu, Yuefeng He, and Yu He contributed equally to this work. We greatly acknowledge the financial support from the Interventional Therapy Clinical Special Research Fund of Chengdu High-Tech Medical Association (Grant No. 2024022). The authors thank Figdraw (www.figdraw.com) for their help in creating the images.

Data Availability

The datasets used and/or analysed during the current study are available from the corresponding author on reasonable request.

References

1. Cao L, Huang WD, Yin LL, Liang Y, Li WH, Liu CR, Xie P, Li ZA, Lu T, Huang XQ, et al. Nanotechnology-driven innovations in transarterial chemoembolization for hepatocellular carcinoma: A focus on smart and flexible platforms. Chin Chem Lett. 2026;37:8.
2. de Galarreta MR, Lujambio A. Hepatocellular carcinoma: killing one bird with two stones. Gut. 2019;68(9):1543–4.
3. Bifulco M, Ciaglia E. Cannabinoid receptor 1 antagonism in hepatocellular carcinoma: killing two birds with one stone. Eur J Gastroen Hepat. 2015;27(6):747–8.
4. Wu S, Fan K, Yang Q, Chen Z, Hou Y, Zou Y, Cai W, Kang L. Smart nanoparticles and microbeads for interventional embolization therapy of liver cancer: state of the art. J Nanobiotechnol. 2023;21(1):42.
5. Dai QX, Wang L, Shao SL, Jia ZK, Rizvi SFA, Gao X, Teng ML, Chen H, Ren E, Chu CC, et al. X-Ray Triggered Phase SHIFT in Radiosensitizer-Lipiodol Formulation for Controlled Synergistic TAE-XDT Cancer Therapy. Adv Funct Mater. 2025;35:43.
6. You R, Yin G, Xu H, Zhu X, Zhang Q, Wang Q, Cao C, Lu Y, Jiang H, Liu J et al. Camrelizumab in combination with TACE for the treatment of unresectable hepatocellular carcinoma (HCC): A multicenter, single-arm, prospective real-world study. J Clin Oncol *39* (15_suppl), e16114–16114.
7. Foerster F, Kloeckner R, Reig M, Chan SL, Chung JW, Merle P, Park J-W, Piscaglia F, Vogel A, Gaillard V et al. ABC-HCC: A phase IIIb, randomized, multicenter, open-label trial of atezolizumab plus bevacizumab versus transarterial chemoembolization (TACE) in intermediate-stage hepatocellular carcinoma. J Clin Oncol *40* (4_suppl), TPS498–498.

8. Yuan G, Liu Z, Wang W, Liu M, Xu Y, Hu W, Fan Y, Zhang X, Liu Y, Si G. Multifunctional nanoplatforms application in the transcatheter chemoembolization against hepatocellular carcinoma. J Nanobiotechnol. 2023;21(1):68.
9. Li J, Lv B, Song L, Zhang X, Zhang J, Ding X, Liu Y, Ye T, Guo M, Fang T, et al. Survival in patients with unresectable hepatocellular carcinoma: TCC cocktail plus TACE vs TACE alone prospective randomized clinical trial. J Translational Med. 2025;23(1):812.
10. Lee SC-ES, Pyo AHA, Koritzinsky M. Longitudinal dynamics of the tumor hypoxia response: From enzyme activity to biological phenotype. Sci Adv *9* (47), eadj6409.
11. Loo SY, Toh LP, Xie WH, Pathak E, Tan W, Ma S, Lee MY, Shatishwaran S, Yeo JZZ, Yuan J et al. Fatty acid oxidation is a druggable gateway regulating cellular plasticity for driving metastasis in breast cancer. Sci Adv *7* (41), eabh2443.
12. Martin SP, Fako V, Dang H, Dominguez DA, Khatib S, Ma L, Wang H, Zheng W, Wang XW. PKM2 inhibition may reverse therapeutic resistance to transarterial chemoembolization in hepatocellular carcinoma. J Experimental Clin Cancer Res. 2020;39(1):99.
13. Cao L, He Y, Li WH, Gong B, Lin H, Shi JL, Yong Y, Wu WC. A Pancreatitis-Inspired Trypsinogen Nanoplatform Reprograms Tumor-Associated Macrophages via NF-κB for Pancreatic Cancer Immunotherapy. Adv Sci 2026.
14. Pu Y, Zhou B, Bing J, Wang L, Chen M, Shen Y, Gao S, Zhou M, Wu W, Shi J. Ultrasound-triggered and glycosylation inhibition-enhanced tumor piezocatalytic immunotherapy. Nat Commun. 2024;15(1):9023.
15. Zheng L, Li H, Guo C, Hu H, Li F. Efficacy and safety of anlotinib combined with TACE among patients with intermediate and advanced-stage hepatocellular carcinoma (HCC). J Clin Oncol *40* (4_suppl), 454–454.
16. Wu WC, Pu YY, Yao HL, Lin H, Shi JL. Microbiotic nanomedicine for tumor-specific chemotherapy-synergized innate/adaptive antitumor immunity. Nano Today 2022, *42*.
17. Ban FQ, Gauld JW, Boyd RJ. Modeling the action of an antitumor drug: A density functional theory study of the mechanism of tirapazamine. J Am Chem Soc. 2001;123(30):7320–5.
18. Xue PP, Bai TJ, Zhuang HL, All AH, Yan SQ, Zeng XM. Cholesterol Metabolism Regulated Nanoliposome Ameliorates Chemo/Photothermal Therapy Reversing CD8 + T Cell Exhaustion. Exploration-Prc 2026, *6* (1).
19. Zhang BB, Zhang J, Li YQ, Li N, Wang YZ, Jang R, Xu XX, Li RF, Chen ZZ, Duan SB, et al. In Situ STING-Activating Nanovaccination with TIGIT Blockade for Enhanced Immunotherapy of Anti-PD-1-Resistant Tumors. Adv Mater. 2023;35:24.
20. Qiao L, Ou Y, Li L, Wu S, Guo Y, Liu M, Yu D, Chen Q, Yuan J, Wei C, et al. H2S-driven chemotherapy and mild photothermal therapy induced mitochondrial reprogramming to promote cuproptosis. J Nanobiotechnol. 2024;22(1):205.
21. Zeng B, Pian L, Liu Y, Wang S, Wang N, Liu C, Wu H, Wan H, Chen L, Huang W, et al. Preparation and effects of functionalized liposomes targeting breast cancer tumors using chemotherapy,

phototherapy, and immunotherapy. J Nanobiotechnol. 2024;22(1):558.

22. Song PY, Chen XH, Liu YC, Fu K, Zhang Y, Wang JW, Zhang L, Shen J, Yang SH, Kong XD, et al. Microenvironment-responsive piezoelectric nanoreactors integrate O and H generation for efficient tumor sonodynamic therapy. Acta Biomater. 2026;217:637–50.
23. Liu LT, Wu Y, Ye JM, Fu QR, Su LC, Wu ZS, Feng J, Chen ZX, Song JB. Synthesis of magnesium nanoparticle for NIR-II-photoacoustic-imaging-guided synergistic burst-like and H cancer therapy. Chem-Us. 2022;8(11):2990–3007.
24. Cao L, Ren L, Yin LL, Xie P, Qiu GY, Lu T, Huang XQ, Li WH, Wu WC, Zhang K et al. A hydrogen generator enhances immunogenic transarterial chemoembolization in hepatocellular carcinoma. *J Control Release* 2026, *392*.
25. Liu SH, Yang HY, Ho MY, Xing BA. Recent Advances of Material-Decorated Photosynthetic Microorganisms and Their Aspects in Biomedical Applications. Adv Opt Mater. 2023;11:11.
26. Gutthann F, Egert M, Marques A, Appel J. Inhibition of respiration and nitrate assimilation enhances photohydrogen evolution under low oxygen concentrations in sp PCC 6803. Bba-Bioenergetics. 2007;1767(2):161–9.
27. Yang JL, Tan SC, Ge SC, Yang MZ, Liu H, Liu W, Zhang KX, Zhang ZZ, Wang ZH, Shi JJ, et al. Cyanobacteria-probiotics symbionts for modulation of intestinal inflammation and microbiome dysregulation in colitis. P Natl Acad Sci USA. 2024;121:52.
28. Ren X, Feng M, Mao M, Long X, Pan J, Tang Y, Zhou P, Peng T, Wang H, Yang F. Cyanobacteria for environmental, energy and biomedical application: a review. Environ Chem Lett. 2025;23(2):491–515.
29. Wu W, Pu Y, Gao S, Shen Y, Zhou M, Yao H, Shi J. Bacterial Metabolism-Initiated Nanocatalytic Tumor Immunotherapy. Nano-Micro Lett. 2022;14(1):220.
30. Galle PR, Tovoli F, Foerster F, Wörns MA, Cucchetti A, Bolondi L. The treatment of intermediate stage tumours beyond TACE: From surgery to systemic therapy. J Hepatol. 2017;67(1):173–83.
31. Schöniger-Hekele M, Kettenbach J, Peck-Radosavljevic M, Müller C. Octreotide treatment of patients with hepatocellular carcinoma - a retrospective single centre controlled study. J Experimental Clin Cancer Res. 2009;28(1):142.

Figures

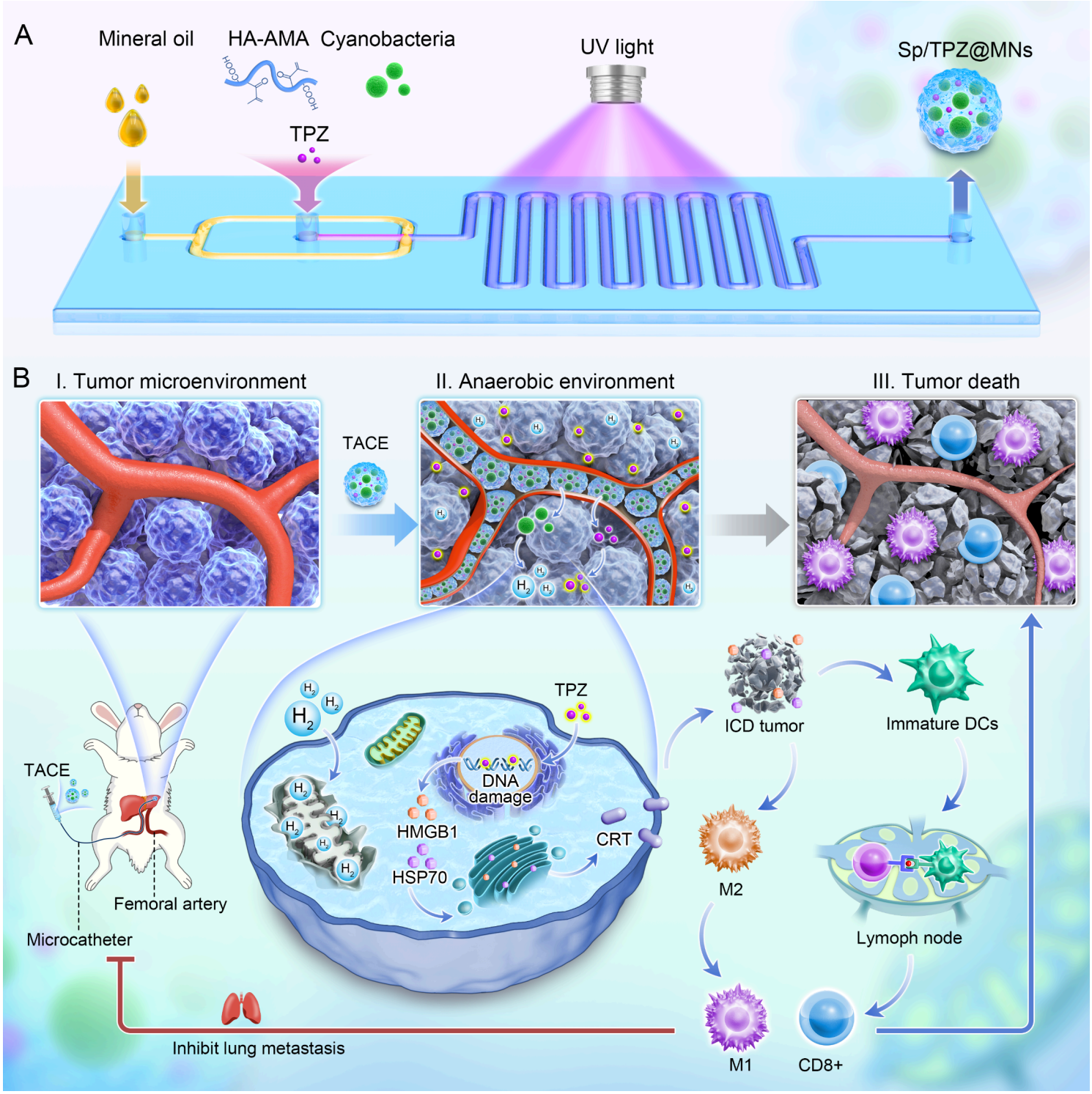

Figure 1

Preparation of Sp/TPZ@MNs and the mechanism of TACE therapy against orthotopic hepatocellular carcinoma. (A) Schematic illustration showing the preparation of Sp/TPZ@MNs. (B) Utilizing TACE-induced intratumoral hypoxia as a trigger, Sp-produced biohydrogen together with activated TPZ elicit ICD and anti-tumor immune responses, restraining HCC growth and metastasis in orthotopic Vx2 tumor-bearing rabbits.

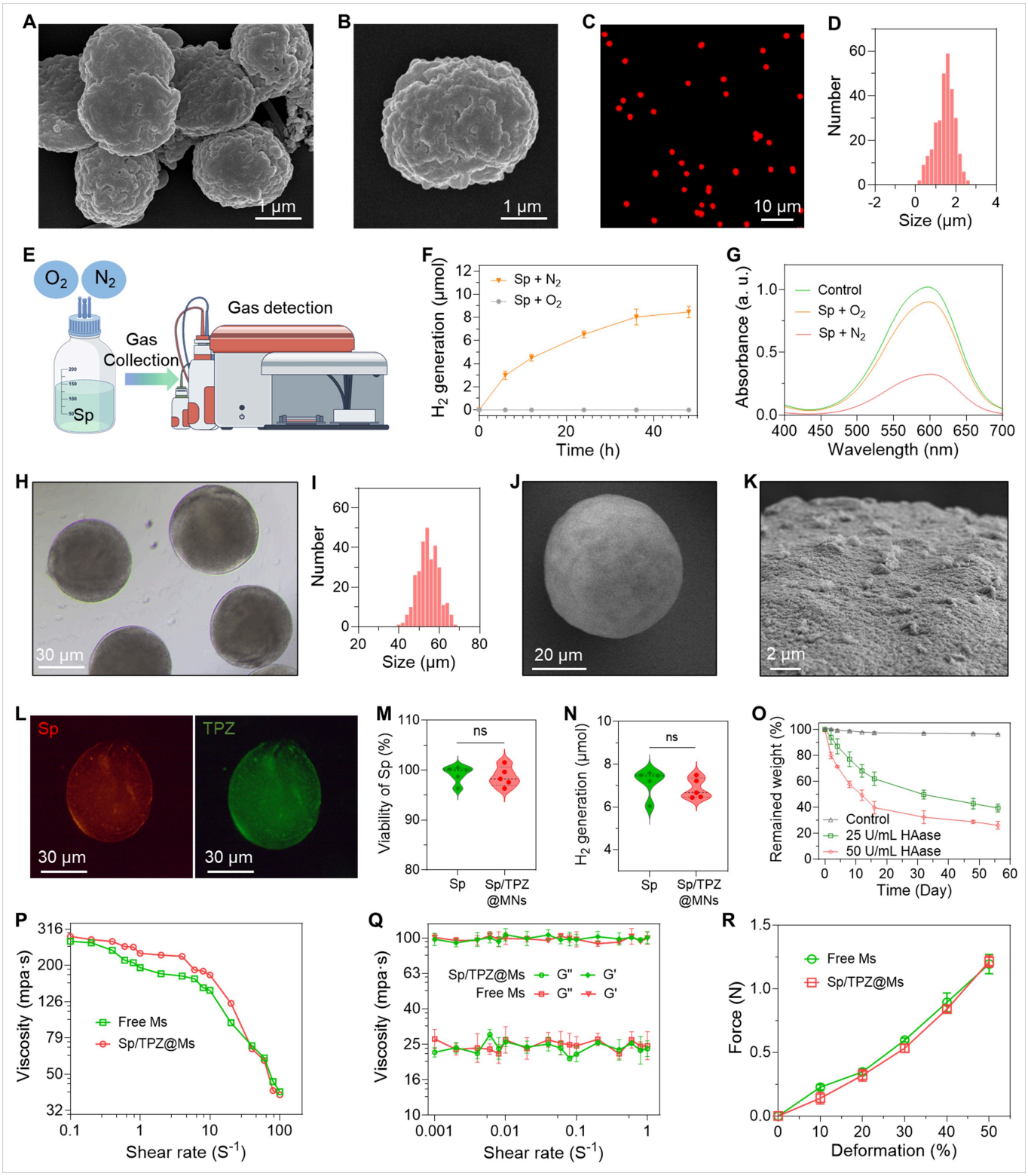

Figure 2

Synthesis and Characterization of the Physicochemical Properties of Sp/TPZ@MNs. (A, B) SEM image of Sp. (C) The laser confocal scanning microscopy image of Sp. (D) Statistical results of the particle size distribution of Sp. (E) Schematic diagram illustrating the detection of hydrogen production by Sp using gas-phase mass spectrometry under different atmospheric conditions. (F) Curves showing changes in hydrogen production by Sp over time under different conditions, as measured by gas-phase mass

spectrometry. (G) UV absorption spectra of methylene blue (MB) after treatment under different conditions. (H) Optical microscope image of Sp/TPZ@MNs. (I) Statistical results of the particle size distribution of Sp/TPZ@MNs. (J, K) Scanning electron microscope image of Sp/TPZ@MNs. (L) LCSM image of Sp/TPZ@MNs, where Sp emits spontaneous red light, and TPZ is replaced with FITC molecules to observe the distribution of both within the microspheres. (M) Survival rates and (N) hydrogen production of free Sp and Sp encapsulated in Sp/TPZ@MNs microspheres after 48 hours of cultivation under identical conditions. (O) Degradation profiles of Sp/TPZ@MNs at hyaluronidase (HAase) concentrations of 25 and 50 U/mL (n = 3 biological samples). (P) Viscosity of free MNs and Sp/TPZ@MNs by shear rate sweeps. (Q) Storage modulus (G') and loss modulus (G") of free MNs and Sp/TPZ@MNs as characterized by oscillatory strain sweeps. (R) Compression force-strain curves of of free MNs and Sp/TPZ@MNs.

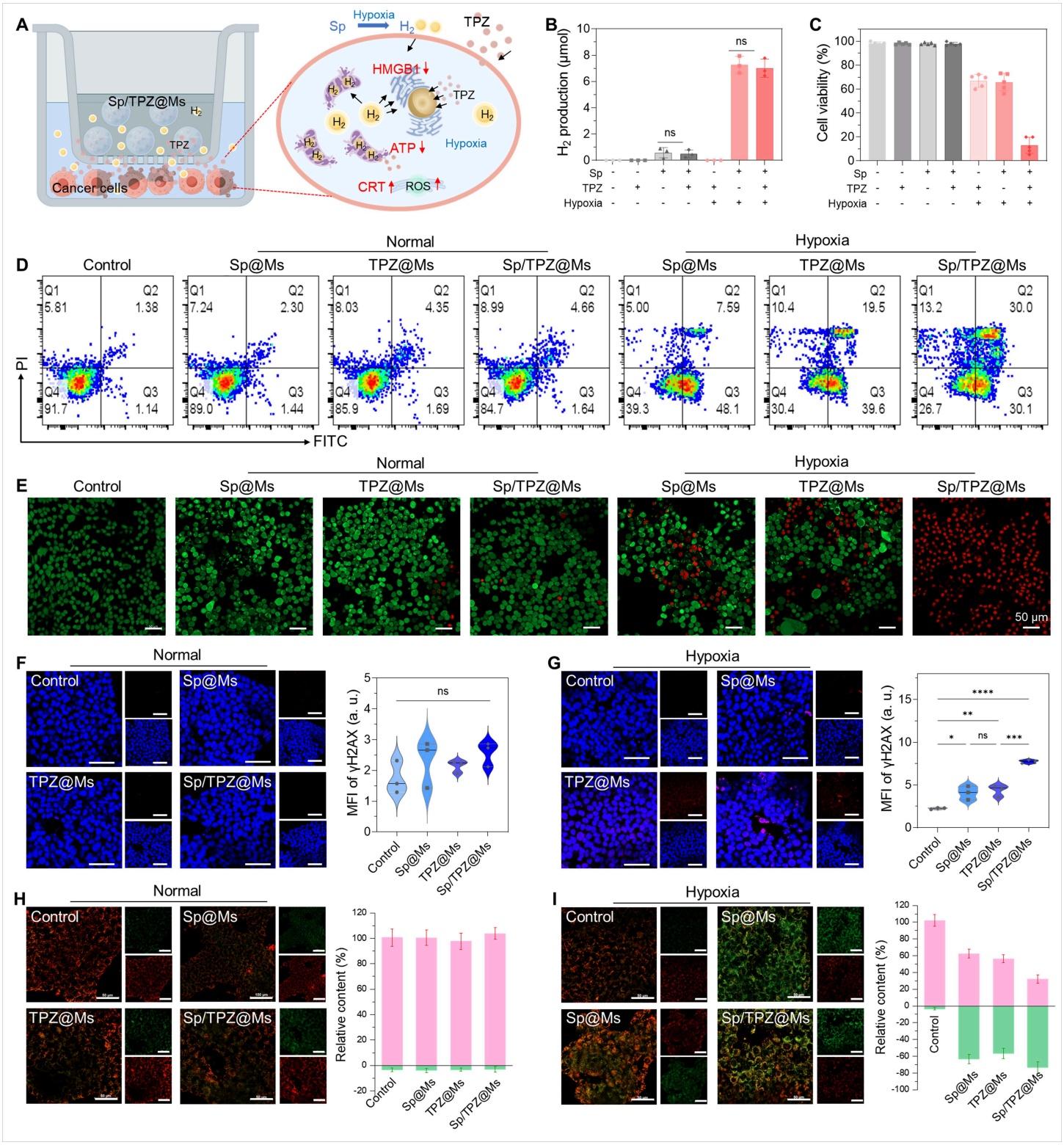

Figure 3

Evaluation of the antitumor effects of Sp/TPZ@MNs at the cellular level in vitro. (A) Schematic illustration of Sp/TPZ@MNs-mediated H_2 generation and TPZ prodrug activation under hypoxia to induce immunogenic cell death in HepG2 cells. (B) H_2 production from different material systems under various conditions. (C) Cell viability of HepG2 cells treated with different gel systems under different conditions was determined by CCK-8 assay, reflecting the killing efficiency. (D) Apoptosis of HepG2 cells induced by

different gel systems under various conditions, as determined by flow cytometry. (E) Live/dead staining of HepG2 cells treated with different gel formulations under various conditions, visualized by confocal laser scanning microscopy (CLSM), with dead cells stained red and live cells stained green. γH2AX staining and quantification of DNA damage in HepG2 cells treated with different gels systems under (F) normoxia and (G) hypoxia condition. ΔΨm assessed by JC-1 staining in HepG2 cells after exposure to various gel systems under normoxic (H) and hypoxic (I) conditions, with quantitative statistics.

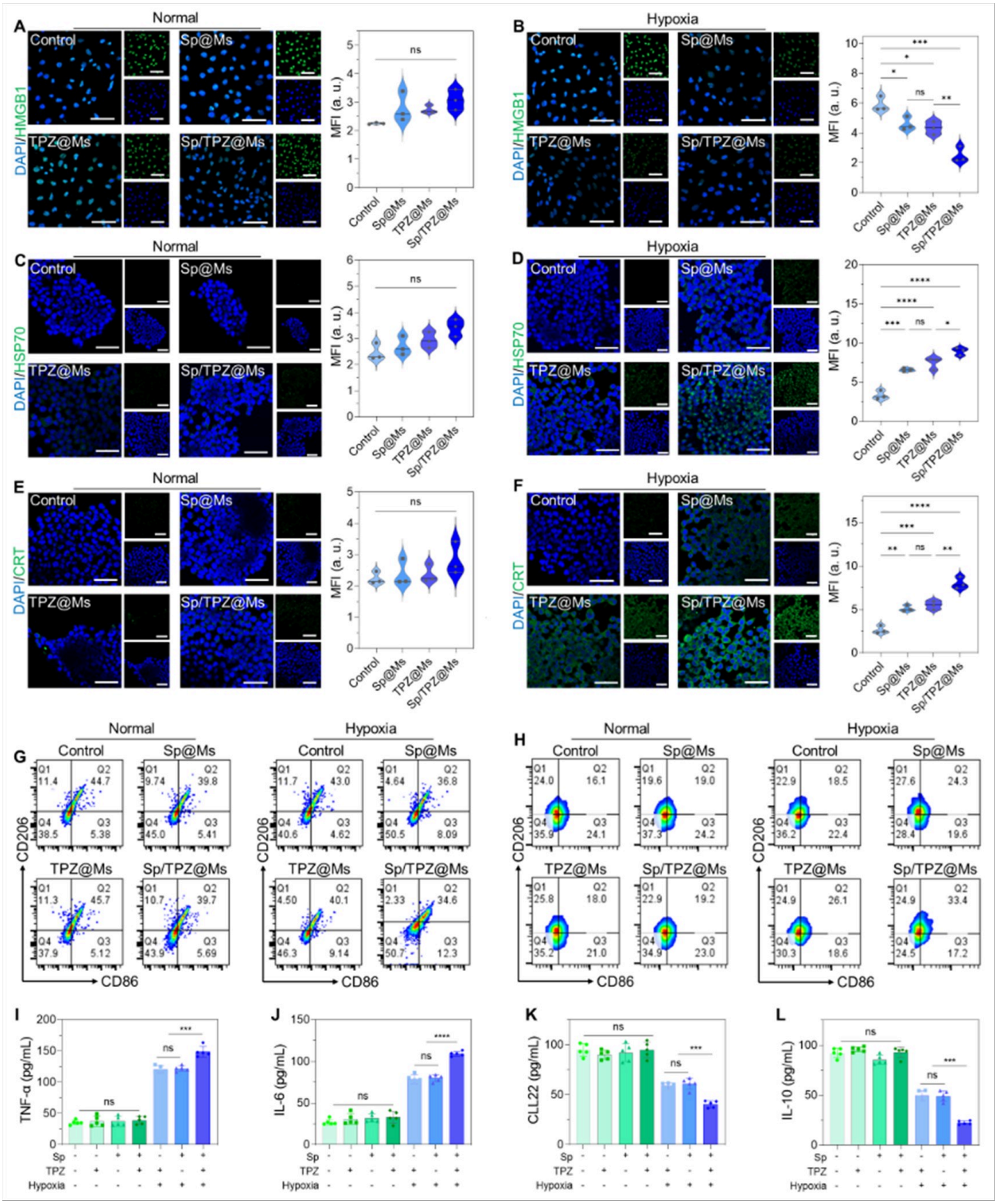

Figure 4

Evaluation of the efficacy of Sp/TPZ@MNs in inducing ICD in HepG2 cells. (A-F) Immunofluorescence analysis of ICD markers, including (A, B) HMGB1, (C, D) HSP70, and (E, F) CRT, in HepG2 cells treated with different gel formulations under normoxia and hypoxia, along with corresponding quantitative statistical results. (G) Flow cytometric analysis of macrophage polarization induced by HepG2 cells pretreated with different conditions. ELISA quantification of (H) CLL22 and (I) IL-10 released by DCs co-cultured with HepG2 cells pretreated under different conditions. (J) Flow cytometric evaluation of DC maturation stimulated by HepG2 cells pre-treated with various gel formulations under normoxia and hypoxia. ELISA quantification of (K) TNF-α and (L) IL-6 70 released by DCs co-cultured with HepG2 cells pretreated under different conditions.

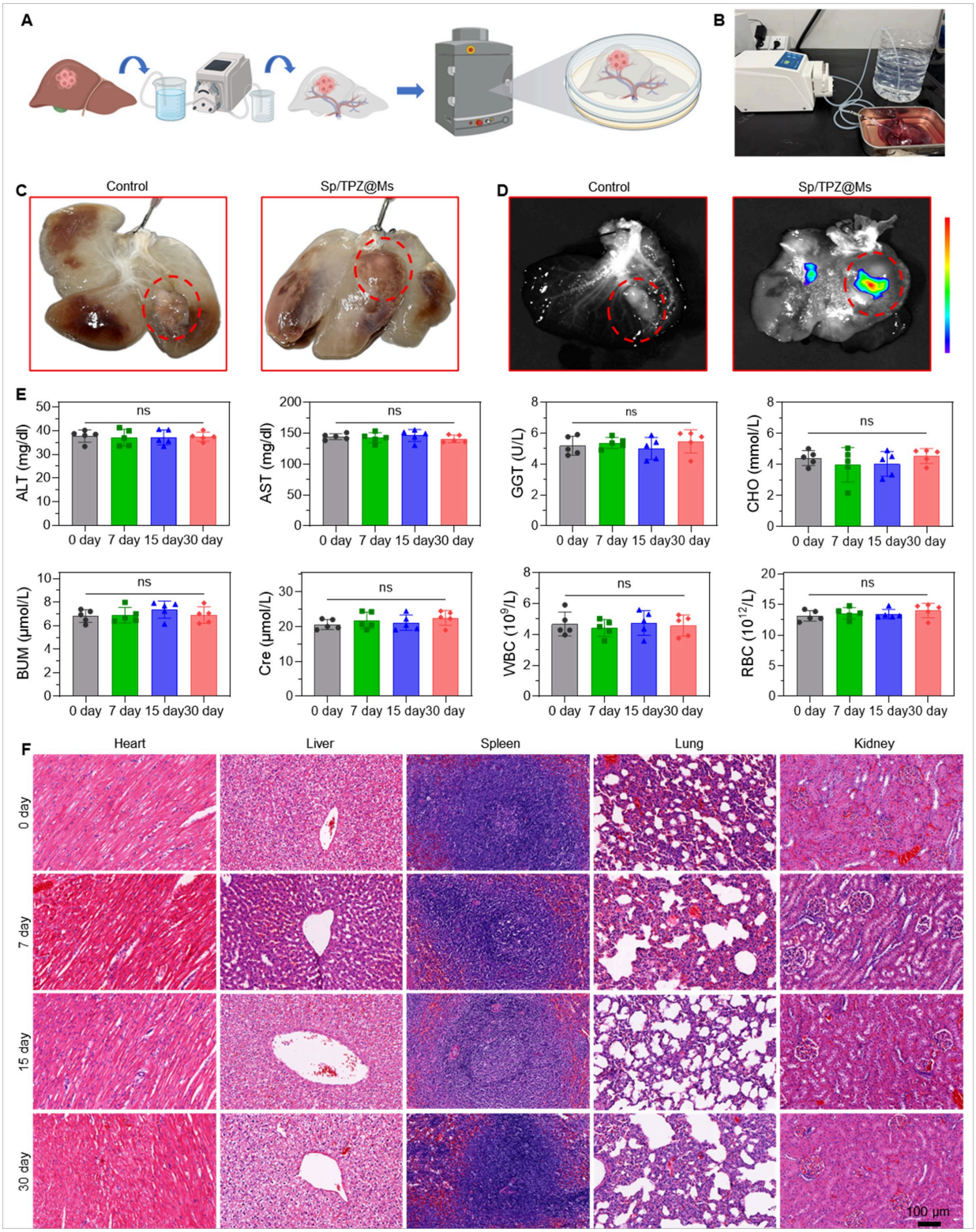

Figure 5

Assessment of the embolization performance and in vivo biosafety of Sp/TPZ@MNs. (A) Schematic illustration of the tissue clearing process for ex vivo liver tissue following embolization with Sp/TPZ@MNs. (B) Digital photographs of the liver tissue clearing process. (C) Representative macroscopic digital photographs of optically cleared liver tumor tissues ex vivo prior to (left) and following (right) Sp/TPZ@MNs treatment. (D) Near-infrared fluorescence images of optically cleared ex

vivo tumor-bearing liver tissues before and after embolization with Sp/TPZ@MNs, in which Sp can emit red fluorescence. (E) Serum biochemical parameters and (F) H&E-stained histological sections of tumor-bearing rabbits at various time points post-embolization with Sp/TPZ@MNs.

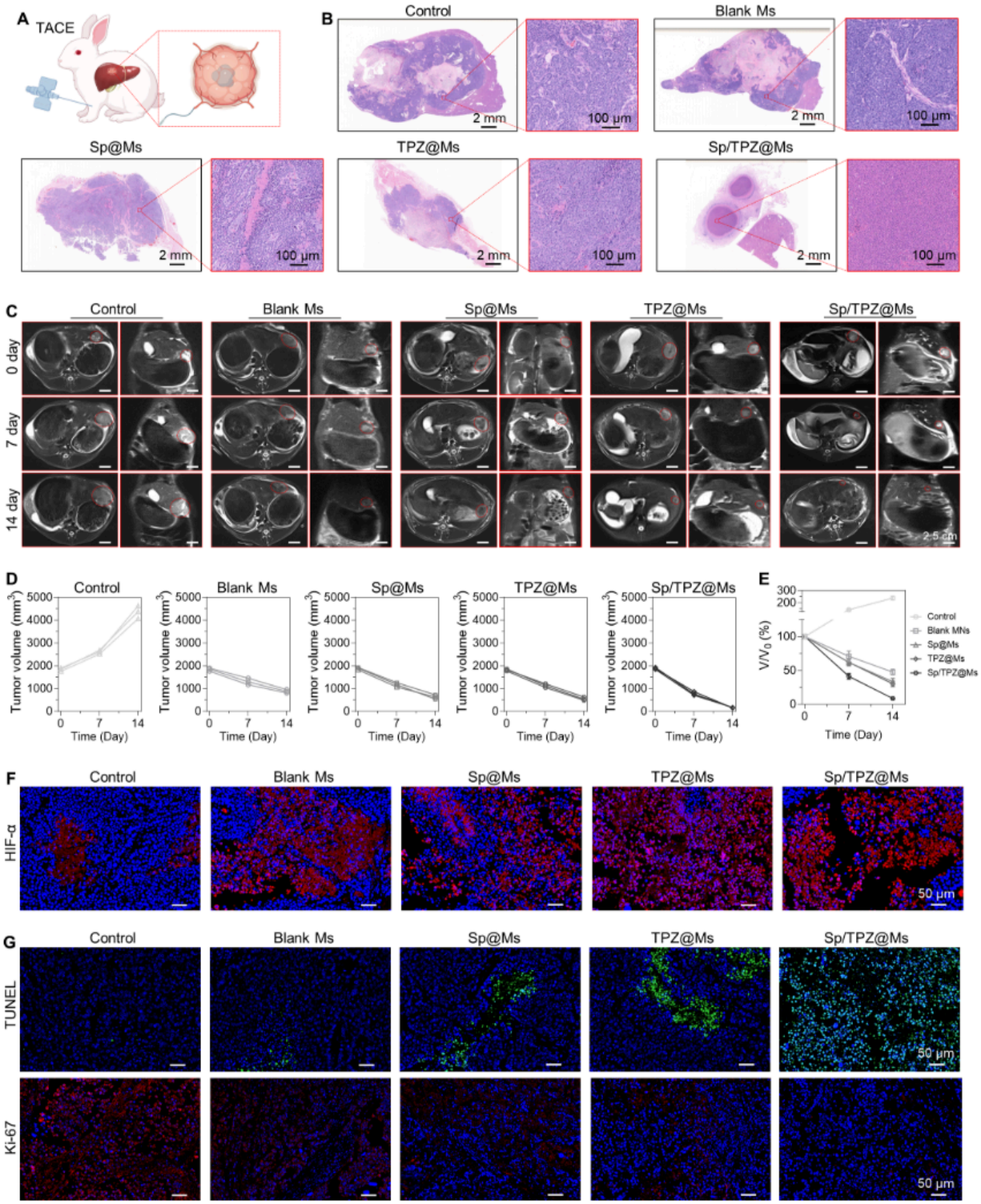

Figure 6

Assessment of the antitumor efficacy of various formulations against rabbit orthotopic hepatocellular carcinoma (HCC). (A) Schematic diagram illustrating the in vivo TACE procedure using Sp/TPZ@MNs in the rabbit orthotopic liver cancer model. (B) Histological images of H&E-stained tumor tissue sections from all treatment groups. (C) T2-weighted magnetic resonance (MR) images of rabbits bearing Vx2 tumors, acquired at designated time points post-TACE with different formulations. (D) Tumor growth curves (individual and mean values) for rabbits in the control and TACE-treated cohorts. (E) Individual tumor growth profiles of rabbits following TACE therapy. Confocal fluorescence micrographs of tumor sections stained for (F) HIF-α and (G) TUNEL/Ki67, respectively.

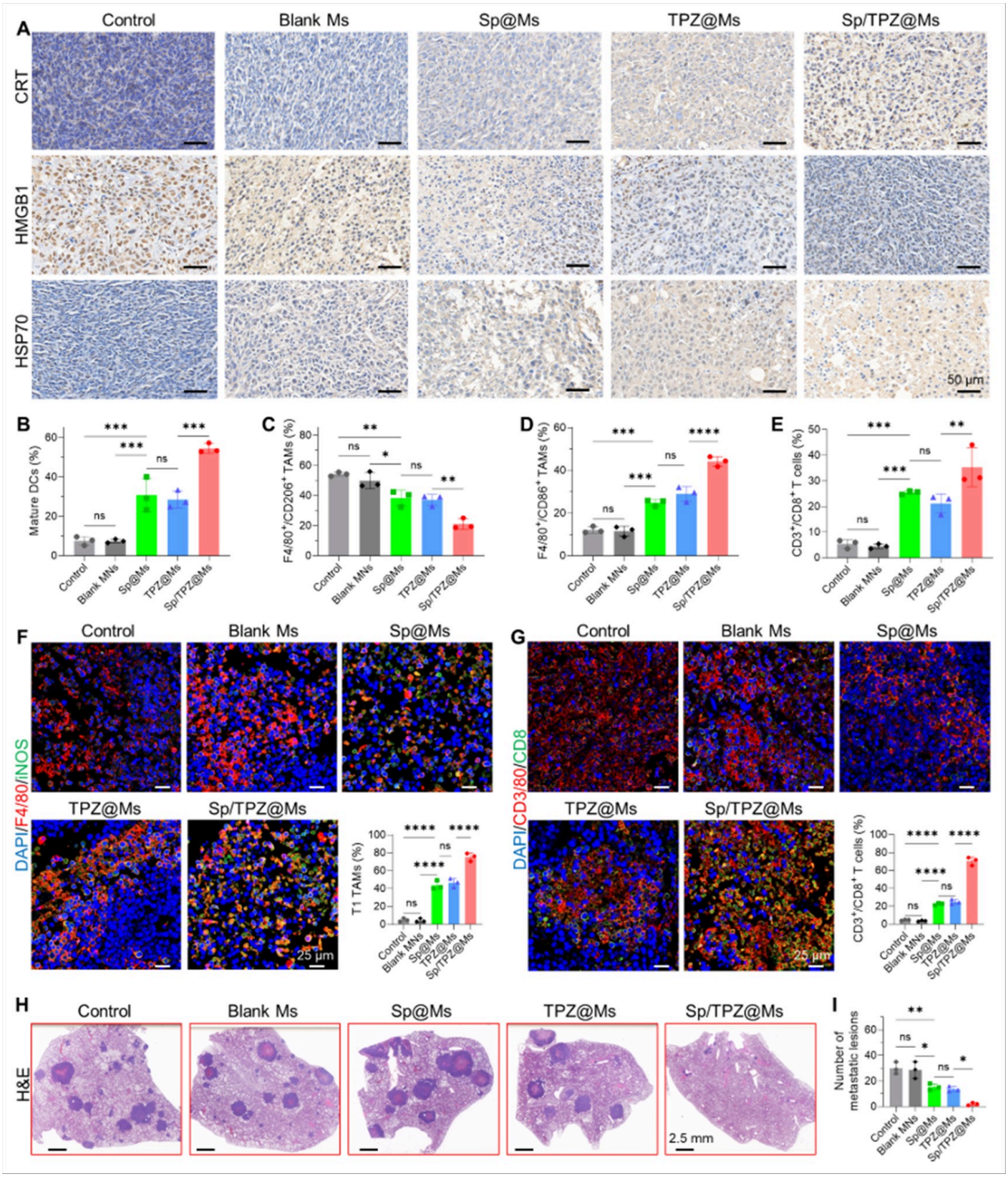

Figure 7

Evaluation of the tumor immune microenvironment following different treatments. (A) Immunohistochemical (IHC) images of CRT, HMGB1, and HSP70 expression in HCC tissues following treatment under different conditions. (B) Flow cytometry analysis of the infiltration percentages of key immune cell populations within tumor tissue, including (B) mature DCs, (C) M1- and (D)M2- TAMs, and (E) $CD8^+$ T cells. Confocal microscopic observations and statistical analysis of (F) $F4/80^+/iNOS^+$ TAMs

and (G) $CD3^+/CD8^+$ T cell infiltration within rabbits' tumors after various treatments. (H) H&E-stained lung sections and (I) quantification of pulmonary metastases in orthotopic HCC rabbits after various treatments.

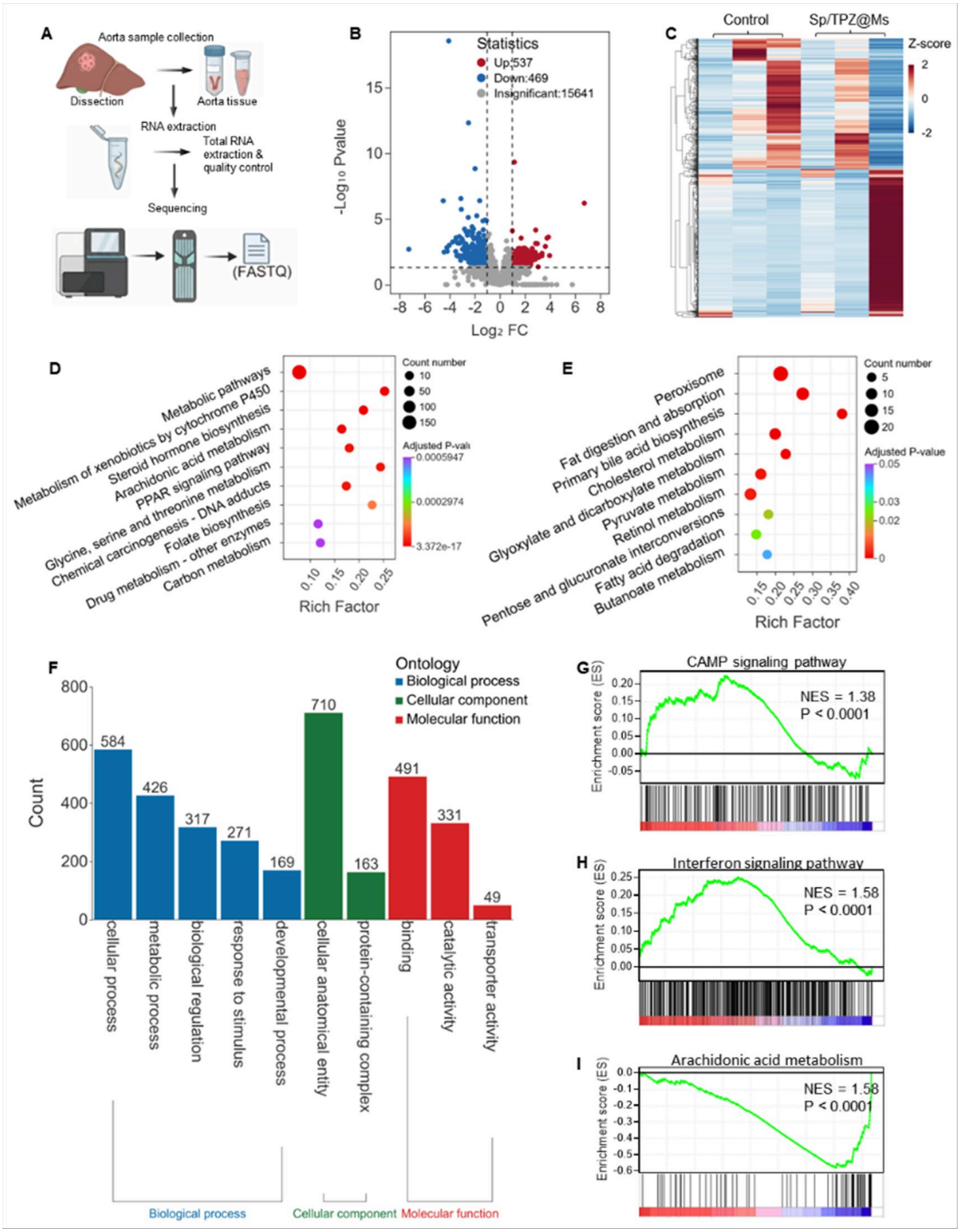

Figure 8

Proposed molecular mechanisms underlying Sp/TPZ@MNs-mediated TACE therapy for orthotopic hepatocellular carcinoma. (A) Schematic of transcriptome sequencing (RNA-seq) workflow on post-TACE tumor samples. (B) Volcano plot of expressed genes in tumors of the Sp/TPZ@MNs group and the control group (Criteria: $|\log_2 FC| > 1$, $P < 0.05$). (C) Heatmap of differentially expressed genes between the Sp/TPZ@MNs group and the control group. Bubble plot of KEGG pathway enrichment analysis for the (D) up regulated genes and (E) down regulated genes. (F) Bubble plot of GO functional enrichment analysis for the DEGs. GSEA of representative signaling pathways about (G) CAMP signaling pathway, (H) interferon signaling pathway, and (I) arachidonic acid signaling pathway after treatment with Sp/TPZ@MNs.

Supplementary Files

This is a list of supplementary files associated with this preprint. Click to download.

- SI.docx